



HHS Public Access

Author manuscript

Nat Cell Biol. Author manuscript; available in PMC 2014 September 01.

Published in final edited form as:

Nat Cell Biol. 2014 March ; 16(3): 224–233. doi:10.1038/ncb2915.

Mechanical Control of the Sense of Touch by β Spectrin

Michael Krieg^{1,2}, Alexander R. Dunn², and Miriam B. Goodman^{1,†}

¹Department of Molecular & Cellular Physiology, Stanford University, USA

²Department of Chemical Engineering, Stanford University, USA

Abstract

The ability to sense and respond to mechanical stimuli emanates from sensory neurons and is shared by most, if not all animals. Exactly how such neurons receive and distribute mechanical signals during touch sensation remains mysterious. Here, we show that sensation of mechanical forces depends on a continuous, pre-stressed spectrin cytoskeleton inside neurons. Mutations in the tetramerization domain of *C. elegans* β -spectrin (UNC-70), an actin-membrane cross-linker, cause defects in sensory neuron morphology under compressive stress in moving animals. Through AFM force spectroscopy experiments on isolated neurons, *in vivo* laser axotomy and FRET imaging to measure force across single cells and molecules, we show that spectrin is held under constitutive tension in living animals, which contributes to an elevated pre-stress in touch receptor neurons. Genetic manipulations that decrease such spectrin-dependent tension also selectively impair touch sensation, suggesting that such pretension is essential for efficient responses to external mechanical stimuli.

Introduction

Due to their location within skin, muscles, joints and other organs, the sensory neurons responsible for touch, pain and proprioception are continually compressed and stretched. To function properly throughout life, these neurons must therefore resist mechanical stress while retaining sensitivity to minute mechanical stimuli. Cells, including neurons, can be stretched slowly without inducing lasting damage. This structural resilience is believed to depend on a membrane-associated cytoskeleton, but little is currently known about the relevant structures or their mechanical properties within neurons *in vivo*. We sought to fill this knowledge gap and investigate how cell mechanics controls touch sensation.

In *Caenorhabditis elegans*, specialized touch receptor neurons (TRNs) are required for sensation of gentle body touch. Physiological studies^{1,2} demonstrate that touch evokes

Users may view, print, copy, download and text and data- mine the content in such documents, for the purposes of academic research, subject always to the full Conditions of use: http://www.nature.com/authors/editorial_policies/license.html#terms

[†]Correspondence to: mbgoodman@stanford.edu.

Author contributions

MK, ARD and MBG conceived the research and designed experiments; MK performed and analyzed experiments; MK, ARD and MBG wrote the paper.

Competing financial interests

The authors declare no competing financial interests.

electrical signals in the TRNs and that such responses trigger a simple escape behavior. The TRNs are well characterized at the molecular and ultrastructural level^{3, 4}, offering a simple system for investigating how mechanical forces govern cell shape and animal behavior. Three anterior (ALML, ALMR and AVM) and posterior TRNs (PLML, PLMR and PVM) tile the body surface and each is surrounded by a specialized extracellular matrix (ECM) and the hypodermal cell⁴. Their non-arborized dendrites are filled with a cross-linked bundle of 15-protofilament microtubules and are approximately 500 μm long and 250 nm wide in adult hermaphrodites⁴. They are closer to the body surface than most neurons and are positioned within 200 nm of the skin or cuticle^{3, 4}. Due to their anatomical location, TRNs could experience significant mechanical strain not only during body touch but also during locomotion, during which *C. elegans* propel themselves forward using rhythmic dorso-ventral contractions.

Here, we investigated the role played by β -spectrin in neuronal cell mechanics and touch sensation, using AVM and ALM as models. To relate mechanics to function, we provide evidence from single cell force spectroscopy and *in vivo* laser axotomy that individual TRNs are under constitutive mechanical tension. We further show that spectrin is required for neuronal pre-stress and is likely to be under tensile load, as revealed by FRET probes that detect piconewton forces⁵. We speculate that tension is important for transmission of mechanical force within TRNs, and show that disrupting the spectrin cytoskeleton reduces sensitivity to external touch.

Results

TRNs are subjected to strain in moving animals

To study how neurons react to mechanical deformations, we monitored AVM shape in crawling worms (Fig. 1a, Supplementary Movie 1). The AVM cell closely follows the body's contour in wild-type animals, shortening during ventral bending and elongating during dorsal bending (Fig. 1b, c) similar to a spring under compressive and tensile forces. These observations imply that AVM experiences compressive stress during ventral bending and tensile stress during dorsal bending, and that the cyclical strains generated during crawling produce little physical damage. Thus, wild-type TRNs are both flexible and resistant to mechanical stress. However, the origin of these properties is not fully understood.

Spectrin is needed for TRN stabilization

In red blood cells, mechanical resilience has long been attributed to a membrane-subjacent, actin-spectrin cytoskeletal network⁶⁻¹¹, and mutations that interfere with network formation cause severe anemia⁷. In the nervous system, spectrin assembles with actin to form cylindrical networks¹⁴ and spectrin mutations cause motor and cognitive disorders¹². β -spectrin has seventeen spectrin repeats flanked by actin-binding and PH domains and forms α/β -spectrin heterodimers through tetramerization domains in β -spectrin repeat 17 and α -spectrin repeat 0 (Ref. 13). Spectrin proteins are conserved in all eukaryotes from protozoa to humans¹⁵ (Supplementary Fig. 1). In *C. elegans*, *unc-70* is the only β -spectrin gene^{16, 17} and is abundantly expressed in neurons.

Because loss of UNC-70 β -spectrin causes movement-induced fractures in motoneurons¹⁸, we reasoned it might protect TRNs from the mechanical stresses imposed during locomotion. Consistent with this idea, we found that AVM collapses into striking undulations during ventral bending (compressive stress, $\varepsilon < 0$) that straighten during dorsal bending (tensile stress, $\varepsilon > 0$) in *unc-70(s1502)* null mutants (Fig. 2a, Supplementary Movie 2). We quantified this buckling phenotype by plotting local AVM curvature against body curvature (Fig. 2b). In wild-type animals, neuron and body curvature were linearly related and tightly correlated under both tensile and compressive stress ($r = 0.94$). By contrast, loss of *unc-70* function increased the variance in neuron curvature and significantly decreased its correlation with body curvature under compressive, but not tensile stress ($r = 0.6$; $p = 1e-13$). This analysis also shows that the largest neuronal deformations were seen at the highest body bends. These findings extend previous observations that UNC-70 β -spectrin is essential for maintaining neuronal integrity in moving worms¹⁸.

We sequenced the entire *unc-70* locus in two mutants, *unc-70(e524)* and *unc-70(n493)*, and discovered that these alleles encode E2008K and L2044P, respectively. Both missense mutations affect highly conserved residues in spectrin repeat 17 (Supplementary Fig. 1), which is critical for tetramerization and network formation^{7, 13, 19, 20}. Because the buckling phenotype was similar in missense and null alleles of *unc-70* (Fig. 2), these data point toward an important yet unrecognized role for the spectrin tetramerization domain in the mechanoprotection of neurons in living animals.

In principle, the undulations present in spectrin mutants could reflect a defect in attachment between the AVM and the hypodermis (the epidermis in *C. elegans*) or cuticle. We reasoned that if detachment were the primary cause of the morphological defects in *unc-70* mutant TRNs, then TRNs would buckle in *him-4* hemiceptin mutants in which the neurite is detached from the surrounding hypodermal cell in due to a lack of functional hemidesmosomes²¹. No buckling was evident in *him-4* mutant animals (Supplementary Fig. 2a, b). We additionally examined the effect of loss of *unc-70* function on the spatial distribution of hemidesmosomes, which occur at regular intervals along the length of the AVM neurite. These structures had a similar organization in *unc-70* and wild-type TRNs (Supplementary Fig. 2c-i)^{21, 22}. Thus, neuron detachment from the hypodermis does not explain the buckling observed under compressive stresses. Because β -spectrin is also present in the hypodermis^{16, 17} that surrounds the TRNs, the buckling instability found in *unc-70* mutant neurons could reflect a loss of spectrin function in the hypodermis. To test for this possibility, we examined transgenic *unc-70* mutants expressing wild-type UNC-70 only in hypodermis. We found that this manipulation decreased, but did not eliminate the buckling phenotype (Supplementary Fig. 3a, c). Next, we asked whether disrupting spectrin networks only in the TRNs could phenocopy the effect of *unc-70* loss of function on neuronal morphology. To do this, we reasoned that over-expressing the tetramerization domain of α -spectrin (repeat 0 and 1) selectively in the TRNs would interfere with spectrin network assembly and act like a dominant-negative mutation. Consistent with this idea, the AVM neurons in these TRN::SPC-1(dn) transgenics displayed compression-induced AVM buckling similar to that observed in *unc-70* mutants (Supplementary Fig. 3b, d).

We propose that the compression-induced undulations in *unc-70* mutants (Fig. 2a, Supplementary Movies 2–4) are analogous of the periodic buckling of an axially compressed flexible beam whose motion is constrained by the surrounding medium²³. In this model of constraint Euler buckling, undulation amplitude increases with the square root of the applied force once the compression exceeds a critical value^{24–26}. Consistent with this model, the buckling amplitude, defined as the maximum off-axis deformation, u_{max} , increased in a nonlinear fashion above a critical value of body strain in *unc-70* mutants (Fig. 2c; Supplementary Note 1). Accordingly, we adapted a model of undulation amplitude and wavelength as a function of the stiffness of the constraining material^{23, 25, 27} and used it to draw inferences about material properties of the neuron and its surrounding tissues. The model links $u_{max}(\varepsilon)$ to the wavelength λ of the undulations and a critical strain ε_c (Ref. 24, 25):

$$u_{max}(\varepsilon) = \begin{cases} \frac{\lambda}{\pi} \sqrt{\varepsilon - \varepsilon_c}, & \varepsilon > \varepsilon_c \\ u_0, & \varepsilon < \varepsilon_c \end{cases} \quad (1)$$

where $u_0=0$ is the buckling amplitude below the critical buckling strain, ε_c . The buckling wavelength λ is inversely proportional to the elastic modulus of the surrounding material^{24–26}. Conversely, the critical buckling strain ε_c is directly proportional to the elasticity and pre-strain within the neurite (see Methods), which we anticipate to arise from the cortical spectrin network in our model neuron. Fitting Equation 1 to the data (Fig. 2c) allowed us to compare λ among wild-type and *unc-70* mutant alleles with wild-type < *unc-70(e524) E2008K* < *unc-70(n493) L2044P* < *unc-70(s1502) Q575stop*. This suggests that the effective elasticity of the TRNs and their surroundings is larger in wild-type neurons than in *unc-70* mutants. Consistent with this idea, expressing wild-type UNC-70 protein in the hypodermis of *unc-70* mutant animals reduces buckling amplitude and wavelength, but is not sufficient to reduce buckling to wild-type levels (*unc-70 > unc-70;Hypo::UNC-70*; Supplementary Fig. 3e). In contrast, TRN-specific interference with network formation after over-expression of TRN::SPC-1(dn) shows that a functional spectrin network in TRNs is necessary for stabilization against compressive forces (Supplementary Fig. 3f). Taken together, these findings establish that UNC-70 β -spectrin has cell autonomous and non-autonomous roles in stabilizing TRNs against crawling-induced forces.

Spectrin-deficient TRNs have altered mechanical properties

The picture emerging from these findings is that β -spectrin protects neurons during compression. To directly investigate the role β -spectrin has in cell mechanics, we measured TRN mechanics with two independent approaches. The first uses an atomic force microscope (AFM) to measure the force required to pull a membrane tether from wild type and mutant TRN cell bodies in culture^{28, 29} (Fig. 3a, b). We found that the force needed to deform the plasma membrane into a highly curved tether was significantly lower in *unc-70* mutant TRNs for a wide range of extrusion velocities (Fig. 3a, b, c). To relate the extrusion force to cell mechanical properties, we fit our force-velocity data to a recent model³⁰, estimated the static force at zero velocity, f_0 , and used these values to compute the apparent membrane tension, T_{app} , which is a sum of the membrane-cytoskeleton adhesion energy (W_0) and in-plane membrane tension (T_m ; Ref. 30, 31). Importantly, we found T_{app} was ~ 10

pN/ μm lower in spectrin mutant TRNs than in wild type cells (Fig. 3d), suggesting that spectrin acts to increase resistance to membrane deformation. Treating TRNs with Latrunculin A or Cytochalasin D (Fig. 3e, f) to disrupt dynamic actin networks had little, if any effect on the static tether force. Taken together, these results show that a functional spectrin network is critical for TRN membrane mechanics and suggest that spectrin may function independently of actin dynamics.

TRNs are under constitutive mechanical tension

Given the difference in T_{app} of 10 pN/ μm and the end-to-end length of spectrin tetramers (100–200 nm^{14, 32}), we can estimate that a tensile force of ~ 1 pN would be applied to each tetramer if the spectrin network were the main element responsible for the reduced tension in *unc-70* mutants. This implies that individual molecules are stretched and that the spectrin network supports mechanical pre-stress in TRNs *in vivo*. Such a pre-stressed neuron will retract following laser axotomy (Fig 4a and Supplementary Fig. 4a) at a rate proportional to the pre-tension^{33, 34}. In wild-type TRNs, little retraction was detected (Supplementary Fig. 4b, c). This could indicate a lack of pre-stress or that attachments between the TRNs and hypodermis prevent retraction *in vivo*. We tested for this possibility by performing axotomies in *him-4* hemicyclin mutants that have defects in TRN attachment, but wild-type touch sensitivity²¹. As shown in Figure 4, TRNs retracted several micrometers in less than one second. Thus, TRNs recoil as expected for a neuron under tension. To determine the contribution of β -spectrin to pre-stress, we analyzed TRN retraction in *him-4;unc-70* double mutant animals. Such double mutant TRNs retracted more slowly and to a lesser extent than *him-4* single mutant neurons (Fig. 4c), indicating that pre-stress is *unc-70*-dependent. Retraction distance and strain rate were also impaired in transgenic animals expressing dominant-negative α spectrin selectively in the TRNs (Fig. 4d), indicating that an intact spectrin network is needed within the TRNs themselves to generate proper longitudinal tension.

β -Spectrin is under tension in living neurites

In principle, β -spectrin could be held under tension or assist other proteins to maintain or generate pre-stress. We used TSMoD, a genetically-encoded molecular force sensor⁵ to directly visualize tension within spectrin molecules *in vivo* and to differentiate between these possibilities. TSMoD consists of a pair of FRET-enabled fluorescent proteins separated by a 40-residue entropic spring derived from spider silk protein⁵, which decreases the distance between the FRET partners in the absence of a tensile force. Accordingly, TSMoD FRET is high in the absence of force or whenever the fluorophores are close together, but decreases if the fluorophores are pulled apart (Fig. 5a). Previous analysis of this sensor indicates that it can resolve forces between 1 and 5 pN⁵. Thus, it is well suited to measure the force across spectrin *in vivo*, which we estimated as ~ 1 pN in our AFM experiments.

Seeking to maximize mechanosensitivity and to minimize disruption of β spectrin, we inserted TSMoD in between the 8th and 9th spectrin repeats of UNC-70 β -spectrin, an interface with high flexibility subjected to force-dependent conformational changes⁸. Next, we expressed this fusion protein from the native *unc-70* promoter in *unc-70(s1502)* null mutants and tested if the resulting transgene rescued the paralysis seen in *unc-70* mutants,

which have an average speed of $7.5 \pm 0.8 \mu\text{m s}^{-1}$ (mean \pm sem, $n = 47$), five times slower than wild-type animals³⁷. The average crawling speed of transgenic animals ($31 \pm 9 \mu\text{m s}^{-1}$, mean \pm sem, $n = 31$) was both significantly faster ($p = 1e-14$, Mann-Whitney U-test) than *unc-70(s1502)* and comparable to wild-type speeds. UNC-70(TSMod) was expressed broadly in many neurons (Fig. 5b) and, as expected for a protein incorporated into a cytoskeletal network, FRAP analysis revealed that this protein was significantly less mobile than cytoplasmic TSMod (Supplementary Fig. 5).

Having established that UNC-70(TSMod) mimics the function of the native β -spectrin, we used it to infer stress within neuronal spectrin networks in living animals. We measured FRET using a pixel-by-pixel sensitized emission technique (see Methods). Since both donor and acceptor fluorophores are present within a single protein, the simplest interpretation of differences in FRET efficiency is that they reflect variation in the proximity of the donor to the acceptor. However, FRET could in principle occur between donor and acceptors present in adjacent molecules. Such intermolecular FRET, if present, is expected to increase with fluorophore concentration. We observed that FRET efficiency was not correlated with acceptor emission (Supplementary Fig. 6a–f), indicating that intermolecular FRET was negligible.

To calibrate our FRET imaging protocol, we replaced the entropic spring in UNC-70(TSMod) with either a stiff linker domain (TRAF) or a short 5 residue linker to generate, mechanically-insensitive, constitutively low and high FRET standards (Fig. 5a): UNC-70(TRAF) and UNC-70(5aa)^{35, 38, 39}. We also measured the FRET efficiency of selected TSMod isoforms using fluorescence lifetime imaging microscopy (FLIM) and found similar values for FRET efficiency regardless of whether they were measured with sensitized emission or FLIM (Supplementary Fig. 6g–j). Moreover, FRET values for the constitutive low and high FRET standards agree with previously published FRET efficiencies derived from fluorescence lifetime measurements^{38, 39}, enabling us to predict relative distances from our FRET efficiency calculations.

With a robust method to quantify FRET as a function of chromophore separation³⁹, we measured neuronal FRET *in vivo* (Fig. 5c). The average FRET efficiency of UNC-70(TSMod) in the TRNs was intermediate between the average FRET efficiency values observed for UNC-70(TRAF) and UNC-70(5aa) (Fig. 5c). UNC-70(TSMod) is expressed in other neurons (Fig. 5b) that had FRET efficiency values similar to the TRNs (Fig. 5c). From this result, we infer that mechanical tension is a shared property of spectrin-expressing neurons. To interpret UNC-70(TSMod) FRET values and deduce whether or not UNC-70 is under tension, we generated two constructs in which TSMod is predicted to experience little or no strain: cytoTSMod, a soluble protein in the cytoplasm and UNC-70(N-TSMod), an N-terminal fusion that places TSMod in a position where it cannot be stretched. Consistent with the hypothesis that UNC-70 is under tension, the FRET efficiency of UNC-70(TSMod) was significantly lower than that found in either of these two constructs (Fig. 5c). We leveraged a prior TSMod calibration⁵ and the FRET efficiency of the UNC-70(TSMod) indicator compared to soluble TSMod to estimate that individual UNC-70 β -spectrin molecules are loaded with ~ 1.5 pN. This value is surprisingly close to the estimate obtained from our *in vitro* AFM assay. Thus, not only is β spectrin required to

maintain tension in TRNs, the molecule itself is held under steady-state pre-stress in neurons *in vivo*.

Next, we determined how manipulations expected to disrupt the spectrin network affect the signals provided by the UNC-70(TSMod) sensor. First, we exploited TRN::SPC-1(dn) to disrupt the spectrin network selectively in the TRNs. As shown in Fig. 5d, this resulted in higher FRET efficiency (decreased tension) in the TRNs compared to other neurites in the same animals. Second, we tested whether laser axotomy could release tension within the spectrin network. We found that UNC-70(TSMod) FRET efficiency increased near the cut site and decreased with distance (Fig. 5e, f). The localized increase in FRET (decreased tension) is specific to the force-sensing fusion protein, since we see no such increase was detected in UNC-70(TRAFF) transgenics (Fig. 5f). Collectively, these data show that individual β -spectrin molecules are under constitutive tension in living neurons and contribute to axonal pre-stress.

Loss of spectrin network function impairs touch sensitivity, but not TRN signaling

Additional functions important for mechanoreceptor function could include mechanical signal transmission via a pre-stressed cytoskeleton⁴⁰. If a pre-stressed spectrin network serves this function, then manipulations that decrease TRN tension should also compromise touch sensitivity. To investigate this possibility, we quantified the touch sensitivity by scoring avoidance responses evoked by stroking individual animals with an eyebrow hair⁴¹ (Fig. 6a). In ten-trial assays, wild-type animals responded significantly better than spectrin mutants (Fig. 6a, b, c), indicating that touch sensitivity was decreased, but not eliminated in spectrin loss of function genotypes. We also tested the influence of spectrin expression in the hypodermis in *unc-70(e524)*, and *unc-70(n493)* mutants. While the hypodermal rescue reduces compression-induced buckling (Supplementary Fig. 3), it had no apparent effect on the touch response in *unc-70* mutants, a result which suggests that the touch defect is due to loss of spectrin dependent tension in the TRNs themselves. Consistent with this idea, the expression of a dominant negative α -spectrin, SPC-1(dn), in the TRNs was sufficient to decrease touch sensitivity (Fig. 6d). Taken together, these data suggest that β -spectrin acts inside the TRNs to increase sensitivity to gentle touch and that proper mechanical tension is essential for mechanosensitivity.

Spectrin-dependent pre-stress could enhance the ability of the TRNs to detect touch or have a more general role in TRN physiology, including synaptic transmission⁴². To differentiate between these possibilities, we obtained transgenic animals expressing channelrhodopsin2 in the TRNs (TRN::ChR2)⁴³. In these animals, TRNs can be activated either mechanically or optically. Consistent with prior studies^{43, 44}, only TRN::ChR2 animals grown with all-*trans* retinal, which is necessary for ChR2 function, reversed direction in response to blue light (Fig. 6e–g). We also found that *unc-70* mutants have wild-type responses to light, but impaired touch sensation. From these data, we infer that loss of β spectrin function has no detectable effect on TRN physiology or neurotransmission, but that β -spectrin enhances sensitivity to touch by regulating mechanical signal transmission.

Discussion

We combined genetic dissection with *in vivo* and *in vitro* analysis of neuronal cell mechanics to show that UNC-70 β spectrin is needed to protect neurons from mechanical stress. Several lines of evidence support the conclusion that TRNs are held under mechanical pre-stress and that the tension is partially borne by a spectrin network. First, *unc-70* mutant AVM neurons buckle in response to compressive stress during movement. Second, we show that an intact spectrin network is essential to maintain tension in the TRNs. Third, FRET measurements with UNC-70(TSMod) establish that spectrin is itself under tension. Importantly, such tension can be decreased by both physical and genetic disruption of the spectrin network in the TRNs. Using genetic and optogenetic dissection, we also show that disrupting the TRN spectrin network impairs touch sensation and leaves synthetic light-activated behaviors intact, a result which suggests that spectrin is needed for mechanical activation of the TRNs, but not for downstream signaling in the TRNs or in the neural circuit linking their activation to behavioral responses. Together, these findings show that spectrin contributes to at least two functions in sensory neurons—mechanoprotection and touch sensation.

How might touch receptor neurons make use of a mechanically pre-stressed spectrin network? Both the hypodermal and neuronal spectrin networks help to protect neurons from mechanical stress and suppress buckling instabilities. By increasing the pre-tension in the neuron, buckling will not occur until the tension is eliminated by the compressive stress, thus providing an effective mechanism for mechanoprotection. The restoring force after a transverse deformation due to a point load is a sum of the pre-stress and elastic contributions⁴⁵. In the limit of small deformations, the elasticity term has little contribution to the total restoring force due to the negligible flexural rigidity of the neuron. Hence, proper spectrin network formation potentially ensures a restoring force and acts as a strain buffer to protect the neuron from damage by during touch and locomotion. If the compressive force, however, exceeds the critical limit and buckling occurs, lateral movement of the neuron will unavoidably deform surrounding tissues. Hence, a higher elasticity of the surrounding hypodermal cell will provide a larger lateral constraint and minimize buckling. Without this additional stabilization, the neuron will undergo significant buckling, as seen in animals lacking both neuronal and hypodermal spectrin networks.

Force transmission has been implicated in several systems involving signal transduction via actin stress fibers⁴⁰, during phototransduction in the fly retina⁴⁶, and sensory mechanotransduction in vertebrate hair cells⁴⁷. Notably, mechanical stimulation during touch in *C. elegans* can activate 20–30 MeT channels within milliseconds¹. Such channels localize to puncta separated by about 2–4 μm^4 , suggesting that signals are transmitted over a distance on the order of 100 μm in less than a few milliseconds. Because pre-stress is known to modulate the transmission speed of mechanical signals in viscoelastic media^{45, 48}, we propose that spectrin-dependent tension may govern rapid channel activation and tune sensitivity to applied stresses. Additional work will be needed to discover whether such transmission occurs primarily by direct connections between spectrin and MeT channels or through spectrin-guided mechanical signal transmission in the plasma membrane.

Since spectrin is a ubiquitous component of the neuronal cytoskeleton from worms to humans and has recently been shown to form a cylindrical network in neurons¹⁴, we hypothesize that pre-stress is an emergent property of the cortical cytoskeleton in neurons that helps to protect neurons from damage and may also serve as molecular stress distributors in sensory neurons embedded in our skin, muscles, joints, and internal organs.

Methods

Strains, genome sequencing, and transgenesis

C. elegans strains were propagated as described⁵⁰ and N2 and TU2769 *uls31* [pMec17::GFP] were used as wild-type controls. A complete list of strains is presented in Supplementary Table 1. All experiments were performed with L4 or young adult hermaphrodites.

The molecular defect in *unc-70(e524)* and *unc-70(n493)* was determined by sequencing genomic DNA isolated from mixed staged worms (gDNA kit, Qiagen). In brief, the fragment corresponding to the *unc-70* locus was amplified with long-range PCR with the primers MK16 and MK09R (Supplementary Table 2). A 9000-bp fragment was isolated and sequenced to reveal a single consistent nucleotide change apparent in each mutant: *unc-70(e524)* encodes G6024A and E2008K, while *unc-70(n493)* encodes T6132C and L2044P (Supplementary Fig. 1).

Young adult worms were injected with constructs of interest (25ng- μl^{-1} or 10ng- μl^{-1}) together with a co-transformation marker (Pmyo-3::mCherry, Pmyo-2::mCherry, or Punc-122::RFP at 2–10 ng- μl^{-1}) and linearized N2 carrier DNA (50ng- μl^{-1}). At least three lines were subjected to initial analyses; results from a single line are presented for clarity. UNC-70 isoforms were injected into *unc-70(s1502);oxIs95* animals, which harbor a null allele of *unc-70* and an integrated transgene that restores wild-type UNC-70 to the hypodermis¹⁸. Strains carrying stable arrays were crossed with N2 Bristol to create strains carrying the same array in both the *unc-70(s1502)* and N2 backgrounds. Transgenic expression of UNC-70(TSMod) in *unc-70(s1502)* mutants partially rescued locomotion and touch defects. Other transgenics were created in an N2 wild-type background.

Constructs for transgenic expression

Wild-type UNC-70—A plasmid encoding wild-type UNC-70 was built as follows. First, RNA was extracted from mixed stage worms (TRIZOL, Ambion RNA isolation kit), eluted in RNase-free water, and used as template for RT-PCR (VILO cDNA kit, Invitrogen), which was conducted in the presence of RNase inhibitor (Superrase, Ambion). *unc-70* cDNA was isolated in two fragments: a 5' 3200 bp fragment was amplified with primers MK16 and MK12R and 3' 3600 bp fragment was amplified with primers MK13F and MK09R. The two fragments were joined using overlap extension PCR (Phusion polymerase, NEB) and blunt-cloned into a pCR Blunt sequencing vector (Invitrogen). Sequencing this product revealed that it corresponds to the major transcript encoded by *unc-70*, K11C4.3a, which is expressed in adult neurons, hypodermis and muscles^{17, 18}.

The endogenous *unc-70* promoter was isolated from genomic DNA using primer pair MK17, which contains a HindIII site and an SpeI site, and cloned into the pCR Blunt vector to create pCR:pUnc70. Both, pCR:pUnc70 and *unc-70* cDNA were digested with HindIII and SpeI to create pCR:unc70E containing the endogenous promoter fused to the full-length *unc-70* open reading frame. In a last step, *unc-54* 3'UTR was inserted into pCR:unc70E and injected into *unc-70(s1502);oxIs95* transgenic animals together with co-transformation marker, Pmyo-3::mCherry *unc-70(s1502);oxIs95* mutant animals expressing full-length *unc-70* cDNA showed a complete rescue of the uncoordinated (Unc) phenotype associated with *unc-70* (not shown).

UNC-70(TSMoD)—The tension sensor, TSMoD⁵, was inserted into UNC-70 in between spectrin repeats 8 and 9, following residue 1166. This was accomplished with a four-way GatewayTM recombination strategy. The four entry clones contained: (1) *unc-70* promoter, as described above; (2) the N-terminal fragment of *unc-70* (encoding residues 1-1166), (3) TSMoD and (4) the C-terminal fragment of *unc-70* (encoding residues 1167-2267) fused to the *unc-54* 3'UTR. The fragments were amplified by PCR using primers 1–8 (Supplementary Table 2) and combined with the appropriate DONR vector in a standard BP reaction, yielding four Entry clones: pENTR Unc70P[1 5], pENTR ATG-R8[5 4], pENTR TSMoD[4 3] and pENTR R9-TAA[3 2]. These clones were combined in a standard LR reaction overnight with pDEST14 (Invitrogen) yielding the assembled construct Punc-70::UNC-70(1 to 1166)::TSMoD::UNC-70(1167 to 2267)::unc-54 3' UTR, which was verified by sequencing.

High FRET (5aa), low FRET (TRAF), cytoTSMoD, and N-TSMoD—Constitutively high FRET and low FRET constructs were made by replacing the TSMoD sensor in UNC-70 with mTFP-Venus FRET pair separated by a 5aa linker or a TRAF domain, respectively^{35, 38}. Entry clones were made as described above, yielding pENTR TSMoD5aa[4 3] and pENTR TSMoDTRAF[4 3].

Cytoplasmic TSMoD (cytoTSMoD) was isolated from pENTR TSMoD[4 3] using the MK42 primer pair and cloned into pCR pUnc70E using the restriction sites SpeI and NsiI. The *unc-70* cDNA coding sequence in pCR pUnc70E was removed by cutting with SpeI and PstI-HF, leaving the *unc-70* promoter and *unc-54* 3'UTR in the backbone.

An N-terminal fusion of TSMoD to UNC-70 was made as follows: TSMoD was amplified by PCR using primers MK42F and MK43R flanked by SpeI and SalI restriction sites and inserted after the first 15 bp of *unc-70* cDNA under the control of the endogenous *unc-70* promoter. The TSMoD and *unc-70* sequences were separated by a flexible linker consisting of five glycines.

Dominant-negative SPC-1 α spectrin—Single step RT-PCR was performed as described above using primer pair MK42 to amplify a cDNA encoding the first 170 residues of SPC-1 α spectrin, which contains spectrin domains 0 and 1 (Ref. 51). The resulting product was cloned into vector MG115 containing pMEC-17⁵² and a C-terminal mCherry tag.

Dynamics of body and neuron curvature

Image collection—To image neuron dynamics in moving worms at high resolution (Fig. 1, 2 and Supplementary Fig. 2, 3), individual *uIs31 [TRN::GFP]* worms were mounted on 1–2% agarose pads, as described⁵³. Worms were free to move without crawling out of the field of view, allowing diffraction-limited observation of neuron morphology. Still images and short movies (0.5 fps, about 75 s) were collected at 20x magnification on a Leica SP5. These movies were analyzed posthoc to derive the curvature of both the body and the AVM neuron, neuron length, L , and neuron strain, L/L_0 . At least 17 animals and an average of 6.9 still images were examined for each genotype.

Image analysis—Body curvature was calculated as follows: Using Fiji (Ref. 54), the ventral side of the animal was marked with 10–20 individual points between the terminal bulb of the pharynx and the nose. The coordinates were imported into IgorPro (Wavemetrics) to calculate curvature according to:

$$\frac{x' y'' - y' x''}{(x'^2 + y'^2)^{3/2}}$$

Where, x' and x'' are the first and second derivative of the projection in x and y respectively. When the animal bends toward its ventral (dorsal) side, curvature is positive (negative). Body curvature was used together with a model of body deformation (Supplementary Information) to calculate body strain (Fig. 1c).

Neuron (AVM) curvature was measured by modifying the strategy for body curvature to account for bucking observed during ventral flexures in *unc-70* mutants. The neurite was traced with 20–30 points distributed along a ~100 μm segment centered at the nerve ring and the curvature at each point was calculated. The mean \pm standard deviation (SD) of these curvatures yielded one data point (Fig. 2b, Supplementary Fig. 3b). The standard deviation of the neuron curvature in each frame was calculated as a running average of 20 frames and plotted against body curvature (Fig. 2b, Supplementary Fig. 2b, S3b).

Neuron length, L , was determined by tracing the anterior branch of AVM from the nerve ring to the nose. This path was imported into IgorPro and the length and curvature of that path was calculated for several consecutive images in a stack. Neuron length was normalized to yield the effective strain, $(L - L_0)/L_0$, with L as the instantaneous neuron length and L_0 is the length as zero curvature, which was determined by fitting a line to the raw data ($L(c) = L_0 + \chi c$) and estimated from the fit parameters according to $L(0) = L_0$. The slope, χ , is a measure of the compliance (inverse of the stress) of the neuron.

Dynamic AFM force spectroscopy

Primary cell culture—Touch receptor neurons were isolated from wild-type (TU2769 *uIs31*) and mutant animals using standard protocols⁵⁵ and plated onto peanut lectin-coated glass bottom Petri dishes (WillCo). Mixed cultures of embryonic cells were grown for up to 7 days in L-15 medium supplemented with heat-inactivated fetal calf serum (10% v/v),

penicillin (10mg mL⁻¹), and streptomycin (100 units). Individual TRNs were visualized by their expression of GFP (Fig. 3a).

AFM force spectroscopy—We used an AFM designed for cell measurements (Bruker BioScope Catalyst, generous loan of Stephen Minne, Andrea Slade and James Shaw, BrukerNano) mounted on a Nikon Eclipse 2000 equipped for epifluorescence to perform AFM force spectroscopy as described⁵⁶. Cantilevers (Olympus Biolever, 6mN m⁻¹) were coated overnight with peanut lectin (1 mg/mL) in MES buffer (pH 6.0, 50 mM) and calibrated according to a thermal noise method⁵⁷.

Individual TRNs were identified by GFP fluorescence and positioned under a cantilever, which was used to pull membrane nanotubes after 100–900 ms contact time and 400 pN contact force. Interaction frequency was adjusted so that ~20% of all cell-cantilever contacts yielded a nanotube event, a maneuver that ensures that only single tether events were analyzed. Pulling velocity was changed randomly to decrease history effect. No history effect was observed. The number of cells analyzed for each genotype and condition is given in Supplementary Table S3. Force-distance curves were analyzed using a step fitting algorithm⁵⁶. Mean tether force was plotted against extrusion velocity and fit to a recently proposed model³⁰ to estimate the static force, f_0 , which was used to estimate tension

according to $f_0 = 2\pi \sqrt{2\kappa(T_m + W_0)}$ ^{29, 30}, where T_m is the in-plane membrane tension and W_0 is the bilayer-cytoskeleton adhesion energy, and κ is the bending rigidity. The bending rigidity was assumed to be $2.7 \cdot 10^{-19}$ Nm (Ref. 29). Log-log transformed data was used to perform linear regression followed by Tukey-type test on multiple regressions in order to assess statistical significance as a function of genotype. Logarithmically transformed data was well fit by a line with slope 1/3 (not shown) as predicted by the power law³⁰. The p-value is shown in Fig. 3 for individual comparisons under the hypothesis that the elevation of the line is the same. Latrunculin A (1μM) and Cytochalasin D (2μM) were applied to cells, treated TRNs were analyzed by dynamic AFM force spectroscopy and compared to data drawn from untreated neurons analyzed on the same day.

***in vivo* laser axotomy and analysis of neurite retraction**

Young adult wild type and mutant worms were immobilized in a drug-free manner using a 5% agar pad, as described⁵³. All strains used for these experiments (Fig. 4, Supplementary Fig. 4) contained the *uIs31* transgene to drive GFP expression in the TRNs. Immobilized worms were placed on the stage of a laser scanning confocal microscope equipped with two, pulsed Ti:Sa lasers (Prairie Technologies). One laser was used for imaging and the other for axotomy. Both lasers have an average power of 2.7 W (at 860 nm), 190 fs pulse width and a repetition rate of 80MHz. The ablation laser was tuned to 720 nm and GFP imaging was performed at 920nm. The energy per pulse of the ablation laser was attenuated to ~2 nJ and a pulse train of ~2 ms was delivered into the sample through a 60x, 0.9 NA water immersion objective. In order to achieve a focused spot at the sample plane, the ablation laser beam was expanded to fill the back aperture of the microscope lens.

To quantify the evolution of the gap-width vs time, kymographs were binarized, denoised and outlined in Fiji. Measurement of the distance of the two neuronal ends from the outlined

image was performed in IgorPro. The time evolution of the resulting gap width was fitted to a single exponential as described³³.

***In vivo* FRET imaging and analysis**

Image collection—Young adult worms were immobilized without drugs on a 5% agarpad, as described⁵³ and imaged with a 63x/1.32 oil immersion lens on a confocal microscope equipped with an Ar ion laser and avalanche photodiode detectors coupled to an upright microscope equipped for epifluorescence illumination (Leica SP5 II, Leica DM6000). Donor (mTFP) and acceptor (Venus) fluorophores were activated with the 458nm and 514nm laser lines, respectively and collected with photodiode detectors tuned to 465–500nm and 520–570nm, respectively. Detector collection efficiency and linearity was determined by imaging dilute, homogenous FITC solutions (0.001–10%, in logarithmic increments) and based on this measurement the gain on the donor and acceptor sensors were adjusted to 150% and 100% to equalize detection efficiency ϕ_D/ϕ_A . Exact values were determined based on the counts at a given ROI for these settings. Bleed-through factors were determined by imaging transgenic worms with an intact donor (GN495) or acceptor (GN498) fluorophore prior to each imaging session and were 0.37 ± 0.05 for the donor channel and 0.17 ± 0.07 for the acceptor channel.

Three image types were collected for each neurite: 1) acceptor excitation-acceptor emission (I_A); 2) donor excitation-donor emission (I_D); 3) donor excitation-acceptor emission (I_F). Portions of the ALM and PLM neurites were identified for imaging based on animal orientation and morphology; other neuronal ROIs included neurites arranged parallel to the long axis of the worm's body.

Image analysis and estimation of FRET efficiency by sensitized emission—For each micrograph, intensity profiles were computed across the diameter of the neurite of interest and fit by a Gaussian to estimate the background intensity, neurite width, and centerline position. The latter information (width, centerline) was used to determine the relevant ROI for subsequent processing. This process was applied to all images to yield the data required to estimate FRET efficiency by sensitized emission following a linear correction for spectral bleed-through. The FRET efficiency, E was computed on a pixel-by-pixel basis according to:

$$E=100 \cdot \frac{\left(cF \cdot Q_D \cdot \frac{\psi_D}{\psi_A}\right)}{qD + \left(cF \cdot Q_D \cdot \frac{\psi_D}{\psi_A}\right)}$$

Where, cF and qD are the bleedthrough-corrected values for the FRET and donor channels, respectively, Q_D is the quantum yield of the donor chromophore³⁸, and ψ_D/ψ_A is the ratio of the collection efficiencies of the donor and acceptor emission sensors. The uncertainty of each pixel was estimated as described⁵⁸ and pixels with errors >500% were rejected from analysis; the remaining pixels were averaged to yield an average E for each ROI.

To better understand the accuracy of this sensitized emission technique, we also performed fluorescence lifetime imaging microscopy (FLIM) on the same transgenic animals as described³⁸. Briefly, worms were immobilized as described and imaged with an SP5 confocal system equipped with a Becker&Hickl SPC-150 module for time-correlated photon counting. Photons were accumulated for up to 150 frames using a 20x oil immersion lens and <5% transmission of a pulsed Ti::Sa laser at 870nm through a 475/28nm emission bandpass filter.

Fluorescence lifetime histogram was fitted using a double exponential decay function, convolved with a synthetic IRF, to extract the amplitude weighted mean of the two components of the excited state lifetime. The lifetime of the donor by itself (in absence of the acceptor) was measured using mTFP transfected MDCK cells. FRET efficiency was

calculated according to $E=1-\frac{\tau_{DA}}{\tau_{DD}}$ in which τ_{DA} is the lifetime of the donor in presence of the acceptor and τ_{DD} is the lifetime of the donor alone. These independent estimates of FRET efficiency yielded essentially identical values for all TSMoD isoforms tested (Supplementary Fig. 6). Moreover, FRET efficiency values for the low FRET (TRAF) and high FRET (5aa) UNC-70 isoforms are similar to published values derived from *in vitro* measurements of mTFP-TRAF-Venus and mTFP-5aa-Venus³⁵.

FRET imaging following laser axotomy—Transgenic animals expressing UNC-70(TSMoD) and UNC-70(TRAF) were immobilized on the stage of the Leica SP5 imaging station and TRNs were axotomized with a pulsed Ti::Sa laser (2.7W, 860nm) using 70% transmission and were ablated by scanning over a 1024×32 pixel ROI for 200ms and allowed to retract for ~5 s before imaging the proximal end, as described above. A final image was taken to calculate FRET after cutting.

Fluorescence recovery after photobleaching (FRAP)

Transgenic animals were immobilized on agarose pads, as described⁵³ and placed on the stage of confocal microscope. UNC-70(TSMoD) was analyzed with a Leica SP5 II and a 63x/1.3 oil immersion lens. Under the control of FRAP Wizard software, a short segment (2–4 μm long) of a TSMoD-expressing neurite was illuminated at full power for 1.5s at 458nm and 514nm. The same region of interest (ROI) was subsequently imaged for 10 frames at 0.6 *fps* and 20 frames at 0.1 *fps*, exciting the Venus fluorophore. This system lacked the temporal resolution needed to analyze rapid recovery of cytoplasmic cytoTSMoD. Therefore, a Prairie Technologies dual 2-photon microscope was used to image and bleach the neurite of cytoTSMoD simultaneously using 920nm excitation with a 60x/0.9 water immersion lens. A line scan of ~10–20μm in length was imaged at 1000 *fps* for 1s to image the recovery process. Image stacks were analyzed to plot intensity vs. time and fitted

with to $D=\ln(2)\frac{\omega^2}{\tau}$ ⁵⁹.

Immunofluorescence

Animals were fixed and subjected to antibody labeling as described⁴. Fixed animals were treated with anti-myotactin antibodies (MH46, Developmental Studies Hybridoma Bank) at

1:50 dilution in B-PBST (PBS + 0.1% Triton-X100 + 3% BSA), incubated overnight at 4°C, and washed several times in B-PBST. Next, samples were treated with an anti-mouse secondary antibody (Alexa567-tagged, 1:2000, LifeTechnologies) overnight, washed in B-PBST, and mounted in VectorShield, cured for several hours (4°C), and imaged in a Leica SP5 confocal system. Interpunctum interval (IPI) was determined from intensity profiles, as described⁶⁰. The binsize for IPI histograms was calculated according to Freedman-Diaconis rule: $width=3.49N^{0.3}$, where N is the number of observations. Histograms were normalized to yield a probability density function, which were fit by a Gamma-distribution.

Statistical and computational analysis

Unless indicated, computations and statistical analyses were performed using IgorPro 6.04 (Wavemetrics) and image analysis was performed with NIH ImageJ or Fiji software⁵⁴.

Supplementary Material

Refer to Web version on PubMed Central for supplementary material.

Acknowledgments

We thank J. Shaw, A. Slade and S. Minne of Bruker Instruments for generous loan of AFM; Z. Liao for worm injections; D. Ramallo, C. Buckley, A. Olson, J. Mulholland for assistance with microscopy; K. Shen for loan of equipment for worm injection and strain integration; C. P. Heisenberg, K. C. Huang and W. J. Nelson for comments. Confocal microscopy and laser axotomy conducted in the Neuroscience Microscopy Service (NMS, partially supported by NS06973) and the Cell Science Imaging Facility (CSIF) at Stanford. Some strains provided by M. Chalfie, E. Jorgensen, W. Schaefer and the *Caenorhabditis* Genetics Center, which is funded by the NIH Office of Research Infrastructure Programs. Work supported by a Stanford Bio-X IIP award (ARD, MBG), the National Institutes of Health (DP2OD007078 ARD, RO1NS047715 and RO1EB006745 to MBG), the National Science Foundation (No. 1136790, ARD), Stanford Cardiovascular Institute Seed Grant (ARD), Burroughs-Wellcome Career Award at the Scientific Interface (ARD) and a Long-term fellowship from HFSP (MK).

References

1. O'Hagan R, Chalfie M, Goodman MB. The MEC-4 DEG/ENaC channel of *Caenorhabditis elegans* touch receptor neurons transduces mechanical signals. *Nature Neuroscience*. 2005; 8:43–50. [PubMed: 15580270]
2. Suzuki H, et al. *in vivo* imaging of *C. elegans* mechanosensory neurons demonstrates a specific role for the MEC-4 channel in the process of gentle touch sensation. *Neuron*. 2003; 39:1005–1017. [PubMed: 12971899]
3. Chalfie M, Thomson JN. Structural and functional diversity in the neuronal microtubules of *Caenorhabditis elegans*. *The Journal of Cell Biology*. 1982; 93:15–23. [PubMed: 7068753]
4. Cueva JG, Mulholland A, Goodman MB. Nanoscale organization of the MEC-4 DEG/ENaC sensory mechanotransduction channel in *Caenorhabditis elegans* touch receptor neurons. *Journal of Neuroscience*. 2007; 27:14089–14098. [PubMed: 18094248]
5. Grashoff C, et al. Measuring mechanical tension across vinculin reveals regulation of focal adhesion dynamics. *Nature*. 2010; 466:263–266. [PubMed: 20613844]
6. Bennett V, Baines AJ. Spectrin and ankyrin-based pathways: metazoan inventions for integrating cells into tissues. *Physiological Reviews*. 2001; 81:1353–1392. [PubMed: 11427698]
7. Gaetani M, Mootien S, Harper S, Gallagher PG, Speicher DW. Structural and functional effects of hereditary hemolytic anemia-associated point mutations in the alpha spectrin tetramer site. *Blood*. 2008; 111:5712–5720. [PubMed: 18218854]
8. Johnson CP, Tang HY, Carag C, Speicher DW, Discher DE. Forced unfolding of proteins within cells. *Science (New York, NY)*. 2007; 317:663–666.

9. Liu SC, Palek J. Spectrin tetramer-dimer equilibrium and the stability of erythrocyte membrane skeletons. *Nature*. 1980; 285:586–588. [PubMed: 6893219]
10. Sleep J, Wilson D, Simmons R, Gratzer W. Elasticity of the red cell membrane and its relation to hemolytic disorders: an optical tweezers study. *Biophysical Journal*. 1999; 77:3085–3095. [PubMed: 10585930]
11. Waugh RE, Agre P. Reductions of erythrocyte membrane viscoelastic coefficients reflect spectrin deficiencies in hereditary spherocytosis. *The Journal of clinical investigation*. 1988; 81:133–141. [PubMed: 3335631]
12. Xu K, Zhong G, Zhuang X. Actin, spectrin, and associated proteins form a periodic cytoskeletal structure in axons. *Science (New York, NY)*. 2013; 339:452–456.
13. Ikeda Y, et al. Spectrin mutations cause spinocerebellar ataxia type 5. *Nature Genetics*. 2006; 38:184–190. [PubMed: 16429157]
14. Li D, et al. A comprehensive model of the spectrin divalent tetramer binding region deduced using homology modeling and chemical cross-linking of a mini-spectrin. *Journal of Biological Chemistry*. 2010; 285:29535–29545. [PubMed: 20610390]
15. Baines AJ. Evolution of spectrin function in cytoskeletal and membrane networks. *Biochemical Society Transactions*. 2009; 37:796. [PubMed: 19614597]
16. Hammarlund M, Davis WS, Jorgensen EM. Mutations in beta-spectrin disrupt axon outgrowth and sarcomere structure. *The Journal of Cell Biology*. 2000; 149:931–942. [PubMed: 10811832]
17. Moorthy S, Chen L, Bennett V. *Caenorhabditis elegans* beta-G spectrin is dispensable for establishment of epithelial polarity, but essential for muscular and neuronal function. *The Journal of Cell Biology*. 2000; 149:915–930. [PubMed: 10811831]
18. Hammarlund M, Jorgensen EM, Bastiani MJ. Axons break in animals lacking β -spectrin. *The Journal of Cell Biology*. 2007; 176:269–275. [PubMed: 17261846]
19. Bignone PA, Baines AJ. Spectrin alpha II and beta II isoforms interact with high affinity at the tetramerization site. *The Biochemical journal*. 2003; 374:613–624. [PubMed: 12820899]
20. Ipsaro JJ, et al. Crystal structure and functional interpretation of the erythrocyte spectrin tetramerization domain complex. *Blood*. 2010; 115:4843–4852. [PubMed: 20197550]
21. Vogel BE, Hedgecock EM. Hemicentin, a conserved extracellular member of the immunoglobulin superfamily, organizes epithelial and other cell attachments into oriented line-shaped junctions. *Development (Cambridge, England)*. 2001; 128:883–894.
22. Hresko MC, Schriefer LA, Shrimankar P, Waterston RH. Myotactin, a novel hypodermal protein involved in muscle-cell adhesion in *Caenorhabditis elegans*. *The Journal of Cell Biology*. 1999; 146:659–672. [PubMed: 10444073]
23. Landau, LD.; Pitaevskii, LP.; Lifshitz, EM.; Kosevich, AM. *Theoretical Physics*. 3. Vol. 7. Butterworth-Heinemann; 1986. *Theory of Elasticity*.
24. Jiang H, Zhang J. Mechanics of Microtubule Buckling Supported by Cytoplasm. *Journal of Applied Mechanics*. 2008; 75:061019.
25. Xiao J, et al. Mechanics of buckled carbon nanotubes on elastomeric substrates. *Journal of Applied Physics*. 2008; 104:033543.
26. Xiao J, et al. Mechanics of nanowire/nanotube in-surface buckling on elastomeric substrates. *Nanotechnology*. 2010; 21:085708.
27. Brangwynne CP, et al. Microtubules can bear enhanced compressive loads in living cells because of lateral reinforcement. *The Journal of Cell Biology*. 2006; 173:733–741. [PubMed: 16754957]
28. Diz-Muñoz A, et al. Control of directed cell migration in vivo by membrane-to-cortex attachment. *PLoS Biology*. 2010; 8:e1000544. [PubMed: 21151339]
29. Hochmuth FM, Shao JY, Dai J, Sheetz MP. Deformation and flow of membrane into tethers extracted from neuronal growth cones. *Biophysical Journal*. 1996; 70:358–369. [PubMed: 8770212]
30. Brochard-Wyart F, Borghi N, Cuvelier D, Nassoy P. Hydrodynamic narrowing of tubes extruded from cells. *Proceedings of the National Academy of Sciences of the United States of America*. 2006; 103:7660–7663. [PubMed: 16679410]

31. Sheetz MP. Cell control by membrane-cytoskeleton adhesion. *Nature Reviews Molecular Cell Biology*. 2001; 2:392–396. [PubMed: 11331914]
32. Nans A, Mohandas N, Stokes DL. Native Ultrastructure of the Red Cell Cytoskeleton by Cryo-Electron Tomography. *Biophysical Journal*. 2011; 101:2341–2350. [PubMed: 22098732]
33. Kumar S, et al. Viscoelastic Retraction of Single Living Stress Fibers and Its Impact on Cell Shape, Cytoskeletal Organization, and Extracellular Matrix Mechanics. *Biophysical Journal*. 2006; 90:3762–3773. [PubMed: 16500961]
34. Ma X, Lynch HE, Scully PC, Hutson MS. Probing embryonic tissue mechanics with laser hole drilling. *Physical Biology*. 2009; 6:036004. [PubMed: 19411738]
35. Borghi N, et al. E-cadherin is under constitutive actomyosin-generated tension that is increased at cell-cell contacts upon externally applied stretch. *Proceedings of the National Academy of Sciences of the United States of America*. 2012; 109:12568–12573. [PubMed: 22802638]
36. del Rio A, et al. Stretching single talin rod molecules activates vinculin binding. *Science (New York, NY)*. 2009; 323:638–641.
37. Ramot D, Johnson BE, Berry TL, Carnell L, Goodman MB. The Parallel Worm Tracker: a platform for measuring average speed and drug-induced paralysis in nematodes. *PloS one*. 2008; 3:e2208. [PubMed: 18493300]
38. Day RN, Booker CF, Periasamy A. Characterization of an improved donor fluorescent protein for Forster resonance energy transfer microscopy. *Journal of biomedical optics*. 2008; 13:031203. [PubMed: 18601527]
39. Koushik SV, Chen H, Thaler C, Puhl IIIHL, Vogel SS. Cerulean Venus and VenusY67C FRET reference standards. *Biophysical Journal*. 2006; 91:L99–L101. [PubMed: 17040988]
40. Na S, et al. Rapid signal transduction in living cells is a unique feature of mechanotransduction. *Proceedings of the National Academy of Sciences of the United States of America*. 2008; 105:6626–6631. [PubMed: 18456839]
41. Hart, A. *WormBook: the online review of C. elegans biology*. 2006. Behavior.
42. Pielage J, Fetter RD, Davis GW. Presynaptic spectrin is essential for synapse stabilization. *Current Biology*. 2005; 15:918–928. [PubMed: 15916948]
43. Schmitt C, Schultheis C, Husson SJ, Liewald JF, Gottschalk A. Specific expression of channelrhodopsin-2 in single neurons of *Caenorhabditis elegans*. *PloS one*. 2012; 7:e43164. [PubMed: 22952643]
44. Leifer AM, Fang-Yen C, Gershow M, Alkema MJ, Samuel ADT. Optogenetic manipulation of neural activity in freely moving *Caenorhabditis elegans*. *Nature methods*. 2011:1–8.
45. Hwang Y, Barakat AI. Dynamics of mechanical signal transmission through prestressed stress fibers. *PloS one*. 2012; 7:e35343. [PubMed: 22514731]
46. Hardie RC, Franze K. Photomechanical responses in *Drosophila* photoreceptors. *Science (New York, NY)*. 2012; 338:260–263.
47. Peng AW, Salles FT, Pan B, Ricci AJ. Integrating the biophysical and molecular mechanisms of auditory hair cell mechanotransduction. *Nature Communications*. 2011; 2:523.
48. Gdc K. Wave propagation in a thin-walled liquid-filled initially stressed tube. *Journal of Fluid Mechanics*. 1984; 141:289–308.
49. Fang-Yen C, et al. Biomechanical analysis of gait adaptation in the nematode *Caenorhabditis elegans*. *Proceedings of the National Academy of Sciences of the United States of America*. 2010; 107:20323–20328. [PubMed: 21048086]
50. Stiernagle T. Maintenance of *C. elegans*. *WormBook: the online review of C. elegans biology*. 2006:1–11. [PubMed: 18050451]
51. Norman KR, Moerman DG. Alpha spectrin is essential for morphogenesis and body wall muscle formation in *Caenorhabditis elegans*. *The Journal of Cell Biology*. 2002; 157:665–677. [PubMed: 11994313]
52. Shida T, Cueva JG, Xu Z, Goodman MB, Nachury MV. The major alpha-tubulin K40 acetyltransferase alphaTAT1 promotes rapid ciliogenesis and efficient mechanosensation. *Proceedings of the National Academy of Sciences of the United States of America*. 2010; 107:21517–21522. [PubMed: 21068373]

53. Kim E, Sun L, Gabel CV, Fang-Yen C. Long-term imaging of *Caenorhabditis elegans* using nanoparticle-mediated immobilization. *PloS one*. 2013; 8:e53419. [PubMed: 23301069]
54. Schindelin J, et al. Fiji: an open-source platform for biological-image analysis. *Nature methods*. 2012; 9:676–682. [PubMed: 22743772]
55. Strange K, Christensen M, Morrison R. Primary culture of *Caenorhabditis elegans* developing embryo cells for electrophysiological, cell biological and molecular studies. *Nature Protocols*. 2007; 2:1003–1012. [PubMed: 17446899]
56. Krieg M, Helenius J, Heisenberg CP, Müller DJ. A bond for a lifetime: employing membrane nanotubes from living cells to determine receptor-ligand kinetics. *Angewandte Chemie (International ed. in English)*. 2008; 47:9775–9777. [PubMed: 19035533]
57. Hutter JL, Bechhoefer J. Calibration of Atomic-Force Microscope Tips (Vol 64, Pg 1868, 1993). *Rev Sci Instrum*. 1993; 64:3342–3342.
58. Zar, JH. *Biostatistical analysis*. Pearson College Div; 2010.
59. Sprague BL, Pego RL, Stavreva DA, McNally JG. Analysis of Binding Reactions by Fluorescence Recovery after Photobleaching. *Biophysical Journal*. 2004; 86:3473–3495. [PubMed: 15189848]
60. Árnadóttir J, O’Hagan R, Chen Y, Goodman MB, Chalfie M. The DEG/ENaC protein MEC-10 regulates the transduction channel complex in *Caenorhabditis elegans* touch receptor neurons. *Journal of Neuroscience*. 2011; 31:12695–12704. [PubMed: 21880930]

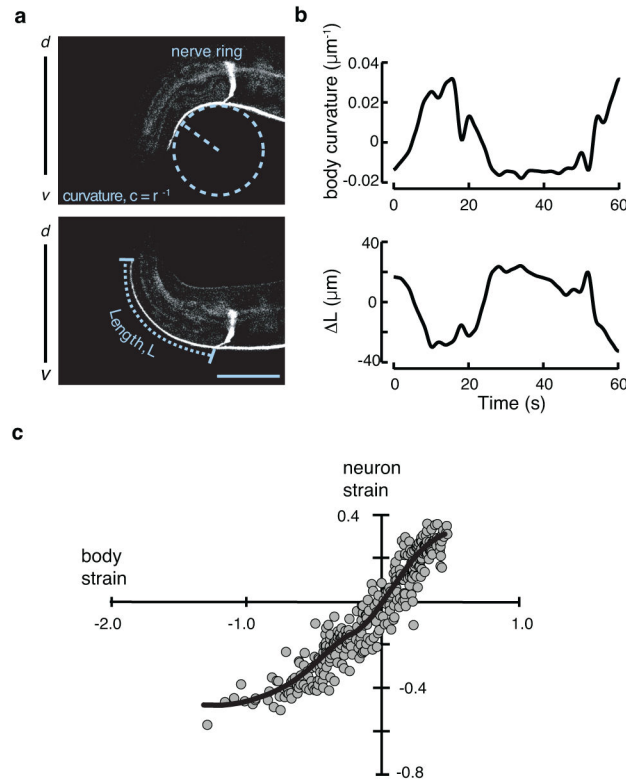


Figure 1. The shape of the touch receptor neuron AVM as a function of stress evoked by body movement

a, Representative micrographs of a GFP-labeled AVM neuron in an adult worm bending ventrally (top) or dorsally (bottom). Curvature and neuron length are schematically indicated as dashed lines. Scale bar = 50 μm .

b, Body curvature (top) and the change in neuron length (bottom) vs. time. Epochs of ventral bending correspond to positive curvature and AVM shortening, while epochs of dorsal bending correspond to negative curvature and AVM extension.

c, Estimated neuron strain, $\Delta L/L$ as a function of body strain. Body strain was derived by approximation of the worm as an Euler-Bernoulli tube⁴⁹, as described in Supplementary Note 1. The black line is a smoothed version of the neuron strain-body strain relationship. Data drawn from $n=7$ control, TRN::GFP transgenic worms and 352 still images collected during four independent imaging sessions.

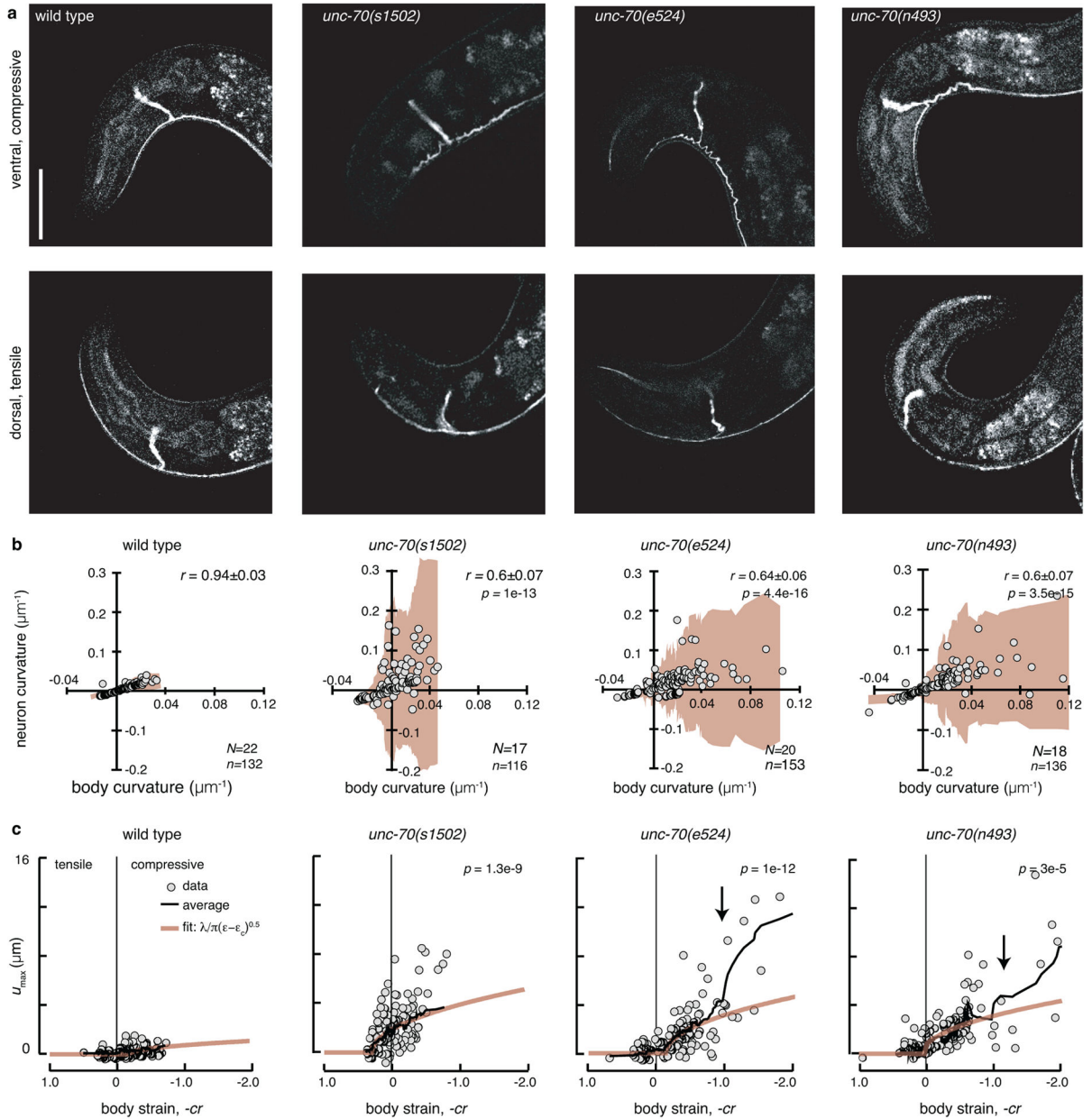


Figure 2. Loss of *unc-70* β-spectrin function causes buckling in TRNs during ventral bending

a, AVM shape during ventral (top) and dorsal (bottom) bending in wild-type and *unc-70* mutant TRN::GFP animals. Scale bar is 50 μm .

b, Neuron curvature vs. body curvature. Each point is the mean of 10–30 adjacent curvature measurements in a still image (see Methods). Shaded areas (beige) indicate the standard deviation of neuron curvature; the increased deviation during compressive (positive, ventral) body bends indicates a larger variation in local neuron curvature. r is the correlation coefficient between neuron and body curvature and r values in *unc-70* mutants were significantly different than wild-type (Fisher z -transform of r). p values indicated in the upper right. N =Number of animals and n =number of still images. Result is from three independent imaging sessions.

c. Maximum off-axis deformation (buckling), u_{max} , of AVM as a function of body strain. Each point is the maximum deformation within a still image. Black lines are running averages of 15 images; beige lines are the calculated buckling deformation of a constrained, flexible filament bundle as a function of compressive strain ε (see Supplementary Note 1). p values derived from linear regression and compared to wild-type indicated in the upper left. Same numbers of observations as in **b**. All strains carry the *uIs31* transgene encoding TRN::GFP.

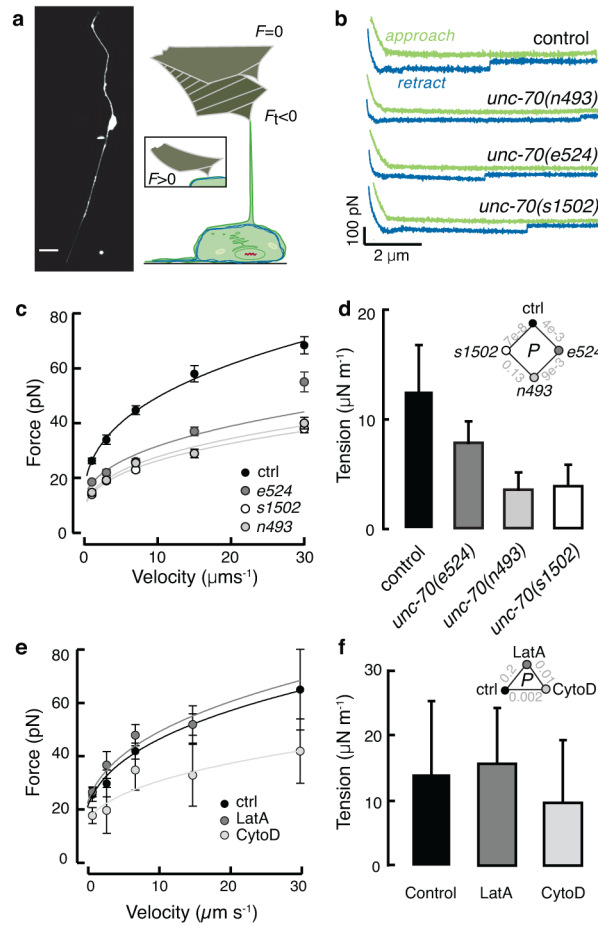


Figure 3. Loss of β spectrin function decreases TRN tension

a, Micrograph of a GFP-tagged TRN *in vitro* (left) and schematic of the tether extrusion procedure. A peanut lectin-coated AFM cantilever was held in contact with each cell for about 400 ms and a lipid tube formed following retraction in about 20% of cases; such events result in a downward deflection of the cantilever ($F_t < 0$).

b, Representative force-distance curves (approach in green, withdrawal in blue) acquired at $7 \mu\text{m}\cdot\text{s}^{-1}$. The discontinuity during withdrawal indicates an interaction event and is proportional to the membrane tension. Similar results were observed in more than 17 cells/genotype.

c, Tether force (mean \pm SEM) vs. cantilever retraction velocity in control and mutant TRNs. Force-velocity curves were fit to a power law and used to estimate the static tether force at zero velocity (see Methods). Supplementary Table 3 lists the number of cells and tethers for each condition. Data in **b** and **c** were acquired during $n=6$ independent AFM sessions.

d, The apparent membrane tension, T_{app} , of cultured TRNs, derived from the static tether force, f_o , estimated from the fits to the data in **c** according to: $T_{app} = f_o^2 / 8\pi\pi^2\kappa$ and a value for the membrane bending rigidity, κ of $2.7\cdot 10^{-19}$ N·m (Ref. 29). Diamond inset shows p values for the tested combinations.

e, Tether force (mean \pm SEM) vs. cantilever retraction velocity in the presence and absence of drugs that disrupt actin. LatrunculinA (LatA) and cytochalasin D (cytoD) applied at 1 and 2

μM , respectively. More than 25 tethers were tested for each speed, except for $30\mu\text{m/s}$ since no data were obtained from LatA-treated cells under this condition. Supplementary Table 3 lists the number of cells and tethers for each condition. Treated and untreated cells were tested in parallel during $n=3$ independent AFM sessions.

f, Membrane tension is unaffected by actin depolymerizing drugs. Triangle inset shows *p* values as a function of treatment. *P*-values derived after log-log transformation of the force-velocity data and linear regression followed by a Tukey-type *t*-test. All strains carry the *uls31* transgene encoding TRN::GFP, which was used to identify TRNs in cultures.

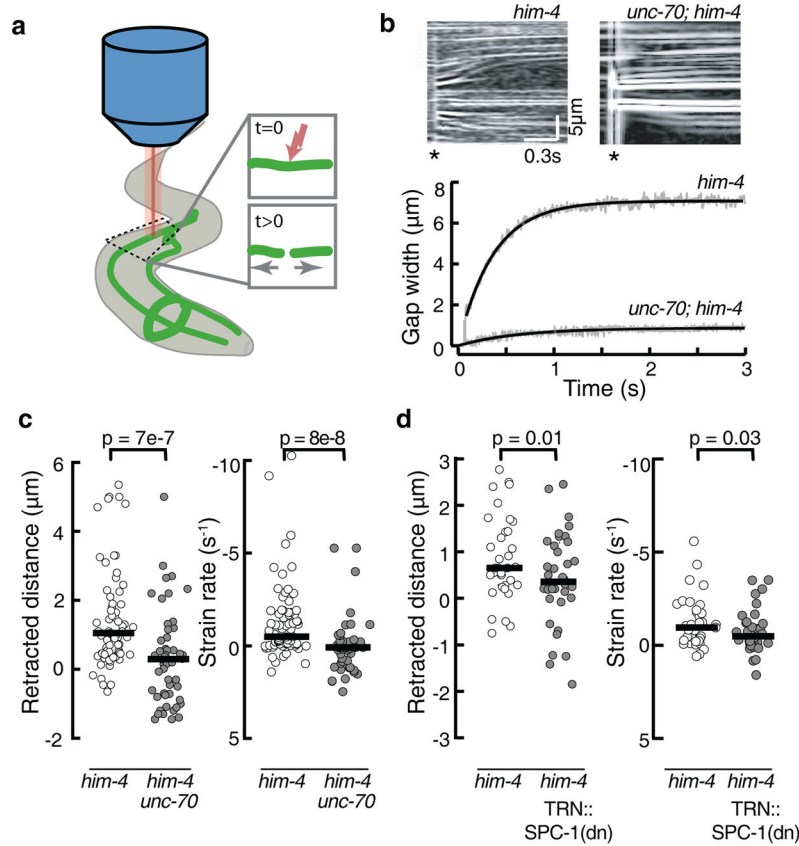


Figure 4. *unc-70(e524)* touch receptor neurons fail to retract after laser axotomy

a. Schematic of the laser cutting experiment. One Ti::Sapphire laser was used to cut TRN axons in immobilized worms, while a second, identical laser was used to simultaneously image the neuron at 1 kHz scan rate.

b. Representative kymographs of control *him-4(e1267)* (top, left) and mutant *him-4(e1267); unc-70(e524)* (top, right) TRNs before and after axotomy. For visualization, kymographs were processed with a Laplace edge detection algorithm to highlight fluorescent speckles. Retraction is evident from the outward motion of fluorescence speckles, which act as fiducial intensity markers. Time runs from left to right. Asterisk indicates time of ablation.

c. Retracted distance, $D_0/2$ (left) and strain rate (right) of control and *unc-70(e524)* mutant TRNs in a *him-4* mutant background after laser cutting. Each point is a single axotomy and thick horizontal bars are the median of 69 and 54 axotomies in 19 control and 22 mutant animals, respectively. Data collected during $n=7$ axotomy sessions. Median values were significantly different (U-test); p values indicated above. Displacement of the two ends was measured from half of the gap width and fit to: $D(t) = D_0(1 - \exp(-\tau t)) + D_a$, where $D(t)$ =gap width as a function of time, D_0 = final gap width, D_a =initial width of the gap immediately after ablation and t =the retraction rate. Fit parameters were used to estimate strain rate³⁴:

$$\gamma \approx -\frac{D_0}{2} \cdot \frac{\tau}{D_a}$$

d, Retracted distance, $D_0/2$ (left) and strain rate (right) of control and TRN::SPC-1(dn) TRNs in a *him-4* mutant background after laser cutting. Each point is a single axotomy and thick horizontal bars are the median of 37 and 38 cuts in 16 control and 13 TRN::SPC-1(dn) transgenic animals, respectively. Data collected during $n=4$ axotomy sessions. Median values were significantly different (U-test); p values indicated above. All strains carry the *uls31* transgene encoding TRN::GFP, which was used to identify TRNs in cultures.

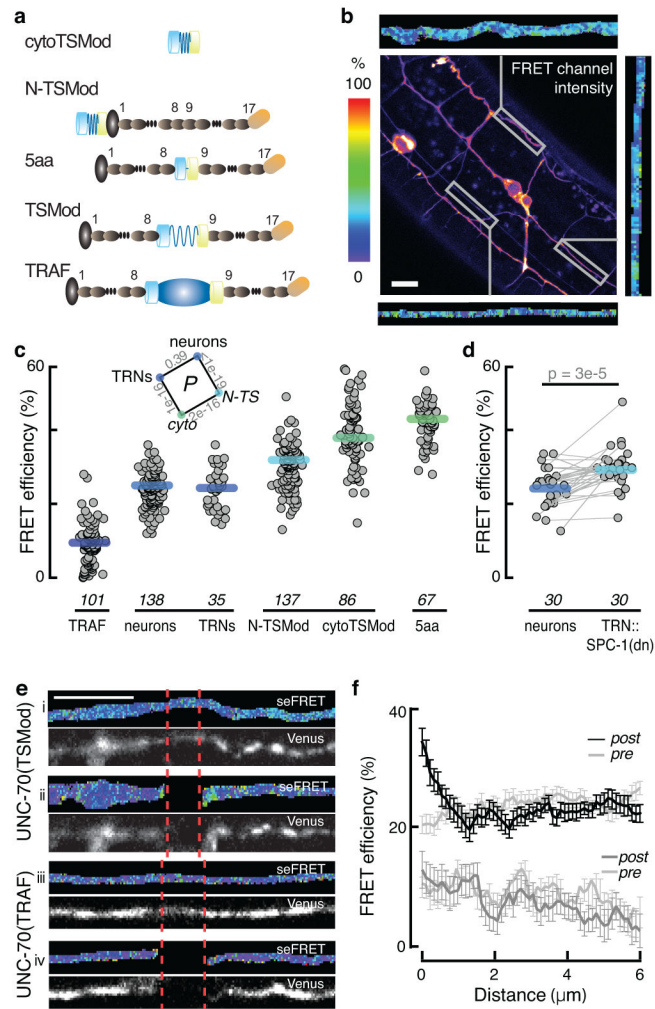


Figure 5. UNC-70 is under constitutive tension in neurons of living animals

a, TSMod-UNC-70 β -spectrin fusion proteins. Shown schematically in descending order of expected FRET efficiency (top to bottom): cytoTSMod, N-TSMod, 5aa, UNC-70(TSMod), and TRAF. Symbols are: mTFP, teal cylinder; spider silk linker, blue spring; Venus, yellow cylinder; UNC-70 actin binding domain, gray oval; spectrin repeats, charcoal oval; TRAF domain, dark blue oval.

b, Representative confocal image of the uncorrected FRET channel after mTFP donor excitation and recording the Venus acceptor emission. Scale bar: 10 μm . Flanking the image are images of FRET efficiency for three ROIs.

c, FRET efficiency of the TSMod fusion proteins illustrated in **a**. TRNs were identified based on their distinctive morphology and position. CytoTSMod and N-TSMod are no-force controls, while UNC-70(5aa) and UNC-70(TRAF) are low and high FRET controls. Each point corresponds to the mean FRET efficiency of a single ROI; thick bars are the median values across ROIs; data collected during eight imaging sessions. Distributions were normal (Jarque-Bera test) and inset shows p -values derived from t -tests for the indicated combinations. The sample size required to estimate the minimal difference between

UNC-70(TSMo*d*) and the no-force controls is 15 at the level of $\alpha=0.01$. The minimum detectable difference for the presented data is $\delta=1.7\%$.

d, FRET efficiency in TRNs and nearby neurons in TRN::SPC-1(dn) transgenics. Lines connect neuron pairs measured in the same animal. *p* value (paired U-test) is shown above.

e, Laser axotomy increases UNC-70(TSMo*d*) FRET adjacent to the cut site. Panels i-iv show representative micrographs of TRNs before (i, iii) and after (ii, iv) axotomy in animals expressing UNC-70(TSMo*d*) (i, ii) or UNC-70(TRA*F*) (iii, iv). Each pair of micrographs shows the FRET efficiency (top) and acceptor fluorescence (bottom). The color scale is the same as in **b** and **c**.

f, FRET efficiency as a function of distance from the cut site. Points are the mean (\pm SEM) of 23 and 17 axotomies for each UNC-70(TSMo*d*) and UNC-70(TRA*F*), respectively. Neurites were imaged at the same position prior to axotomy (gray traces, pre). As expected for an axotomy-induced tension release, FRET was highest near the cut site and declined to control values within 2 μ m. Data collected during *n*=3 imaging sessions.

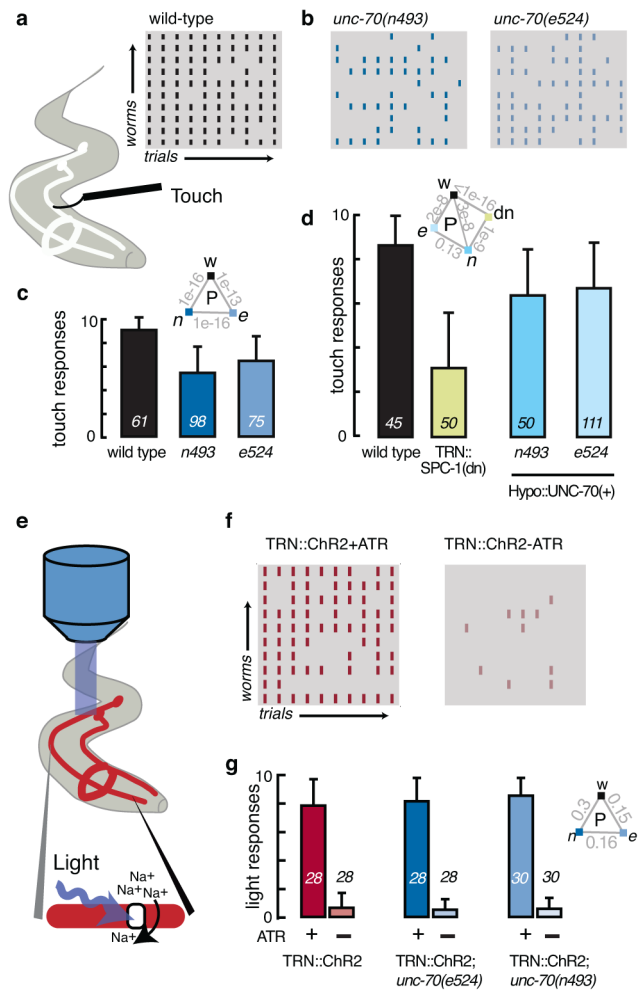


Figure 6. Loss of *unc-70* function impairs touch sensitivity, but not synthetic light sensitivity
a–d, Touch response in wild-type and *unc-70* mutants.

a, Schematic of the assay used to measure touch sensitivity⁴¹ and ethogram of touch responses in wild-type (N2). Rows represent individual worms, columns are trials, and black ticks indicate a stimulus-evoked reversal. (Gray ticks indicate trials that failed to elicit a detectable response.)

b, Ethogram of *unc-70(n493)* and *unc-70(e524)* mutant animals.

c, Average touch response as a function of genotype. Bars are mean \pm s.d., numbers on each bar shown the number of animals tested blind to genotype during four assay sessions; inset shows p values derived from a U-test.

d, Average response rate in transgenic animals with TRN-specific defects in spectrin function (TRN::SPC-1(dn)) or hypodermis-specific expression of wild-type UNC-70. Bars are mean \pm SD, numbers on each bar show the number of animals tested blind to genotype during $n=2$ or $n=4$ assay sessions for TRN::SPC-1(dn) and *unc-70*; HYPO::UNC-70(+) transgenics, respectively; inset shows p values derived from a U-test.

e–g, Light-induced reversal in transgenic animals expressing ChR2 selectively in the TRNs (TRN::ChR2).

e. Schematic of optogenetic stimulation.

f. Ethogram of the response of TRN::ChR2 control animals to blue light in presence (left) and absence (right) of all-trans retinal, ATR.

g. Average light response in control and *unc-70* mutants grown in the presence (green, blue bars) or absence of ATR (gray bars) and stimulated with brief (1s) light pulses of $0.48 \text{ mW}\cdot\text{mm}^{-2}$. Bars are mean \pm SD, number of animals tested during $n=2$ independent assay sessions is indicated near each bar; inset shows p values derived from a Mann-Whitney U-test.